

Kinematic analysis of musculoskeletal structures via volumetric MRI and unsupervised segmentation

José G. Tamez-Peña^a, Saara Totterman^b and Kevin J. Parker ^a

^aDepartment of Electrical and Computer Engineering, University of Rochester,
Rochester, NY, 14627

^bDepartment of Radiology, Medical Center, University of Rochester, Rochester, NY, 14620

ABSTRACT

In this work we present a comprehensive approach for the kinematic analysis of musculoskeletal structures based on 4D MRI data sets and unsupervised segmentation. We applied this approach to the kinematics analysis of the knee flexion. The unsupervised segmentation algorithm automatically detects the number of spatially independent structures present in the medical image. The motion tracking algorithm is able to pass simultaneously the segmentation of all the structures which allows an automatic segmentation and tracking of the soft tissue and bone structures of knee in a series of volumetric images. Our approach requires a minimum of interactivity with the user, eliminating the need for exhaustive tracings and editing of image data. This segmentation approach allowed us to visualize and analyze the 3D knee flexion, and the local kinematics of the meniscus.

Keywords: Motion tracking, Deformable models, Musculoskeletal, Meniscus

1. INTRODUCTION

The ability to evaluate the motion patterns of the articulating bones and the changes in the relationships between soft tissue structures of the joints during motion would greatly increase our understanding of the development and staging of several musculoskeletal related deceases. The whole-volume CT and MRI imaging which provides 3D data, would in theory, give us the ability to evaluate and also visualize those phenomena. However, so far a few studies have been done in this direction. The purpose of this work was to apply an adaptive 4D segmentation algorithm and visualization techniques to display and evaluate the kinematic motion of the knee major structures. Special attention will be taken to the meniscus kinematics during the knee flexing using 3D MRI data. Our final goal is the kinematic analysis of a human joint through a series of MRI scans. There are several anatomical components in the joints where motion analysis is very important, but joint motion is very complex due to the deformations of the soft tissues involved (ie. tendons, ligaments, muscle, etc.). These deformations cause topological changes that make the analysis of MRI images difficult. The segmentation of every frame of a series of MRI images can be very useful for this analysis. Therefore, segmenting these images is the first step in our research.

Although the segmentation of a of images in a sequence can be done by applying an independent segmentation algorithm to each frame on the sequence, there are certain problems in using this approach. First, boundaries between low-contrast structures are not well defined. Thus, noise and sampling make the boundaries found the segmentation algorithms change between series. The second problem resides in the labeling of the image. There are so many structures in a typical medical image, that a consistent labeling at each volume in the sequence is difficult to enforce. Third, a robust segmentation algorithm is computationally demanding; thus, segmenting each volume using this process is not practical. Fourth; it is desirable to utilize lower resolution (or a simple sequence) image sets throughout the sequence in order to speed the data acquisition and analysis. Giving these three objections, we decided to use an alternative approach for the segmentation of a volumetric image sequence based on the segmentation of the first image on the series.

A motion-estimation and tracking algorithm provides the information needed to pass the segmented image from one frame to the other. Since the regions have both rigid and nonrigid components, this has to be taken into account

Further author information: (Send correspondence to J.G.T.)

J.G.T.: E-mail: pena@ece.rochester.edu

S.T.: E-mail: tot@rad.rochester.edu

K.J.P.: E-mail: parker@ece.rochester.edu

when performing the estimation of the 3D motion. Although there has been some research in this area of deformable motion tracking and analysis,¹⁻⁶ most of it concentrates on the time evolution of a single structure in the image. The analysis of joint kinematics involves the motion of many structures making the current approaches unsuitable. Therefore we decided to develop a more general approach. This takes into account the local deformations of the soft tissues by using the *a priori* knowledge of the material properties of the different structures found in the segmentation step. Also, this knowledge allows us to apply two different strategies; one for recovering the rigid motion and another for the soft tissues. Once the selected points have been registered, the motion vectors of every voxel in the image are computed by interpolating the motion vector of these selected points. The estimated motion vector is used to pass the segmentation from one frame to the next. This process is repeated until all the volumes in the sequence are segmented. This approach is basically the motion-tracking algorithm outlined in Tamez,⁷ with some minor improvements on the tracking algorithm. This paper presents the latest results and its applications to the analysis of the joint kinematics.

2. MOTION ESTIMATION

Researchers have proposed the use of deformable models for the analysis of images^{8,1,9} as well as its application to the time evolution analysis.^{2,10,5,11,4,12-15,3} Following a similar approach, our algorithm recovers the point correspondence by minimizing the “total energy” of a mesh of mass-spring system which models the physical properties of the anatomy. This models are a simplification of a solid finite element model and are widely used on simulations.¹⁶ The main difference is that our mesh is not constrained to a single structure in the image, but it models the whole volumetric image. The mesh properties are driven by the original data and the structures material properties. The material properties are assumed to be known and are coded on the segmented data. Basically, our motion estimation approach is a point correspondence recovery algorithm between two consecutive frames.^{17,18,11,19,20}

Many deformable models assume that a force field can be extracted from the image. This force field drives spring attached point masses. Most of them use this approach to build semi-automatic feature extraction algorithms. Using a similar approach, let us assume that the image sampled at $t = n$ is a set of three dynamical scalar fields: $\Phi(\mathbf{x}, t) = \{g_n(\mathbf{x}), \|\nabla g_n(\mathbf{x})\|, \nabla^2 g_n(\mathbf{x})\}$ (the gray value, the magnitude of the image gradient, and a Laplacian of the image), so that a change in the field $\Phi(\mathbf{x})$ causes a quadratic change in the scalar field energy $U_\Phi(\mathbf{x}) \propto (\Delta\Phi(\mathbf{x}))^2$. Furthermore, assume that the underlying structures are modeled as a mesh of springs attached to point masses in a state of equilibrium with these scalar fields. Although equilibrium implies that there is an external force field, its shape is not important in our analysis. Let us assume that the point distribution changes in time. Thus, the total energy change in (Δt) , is:

$$\Delta U_n(\Delta \mathbf{X}) = \sum_{\forall \mathbf{X} \in g_n} \left[\begin{array}{l} \alpha(g_n(\mathbf{x}) - g_{n+1}(\mathbf{x} + \Delta \mathbf{x}))^2 \\ + \beta(\|\nabla g_n(\mathbf{x})\| - \|\nabla g_{n+1}(\mathbf{x} + \Delta \mathbf{x})\|)^2 \\ + \gamma(\nabla^2 g_n(\mathbf{x}) - \nabla^2 g_{n+1}(\mathbf{x} + \Delta \mathbf{x}))^2 \\ + \eta \frac{1}{2} \Delta \mathbf{X}^T \mathbf{K} \Delta \mathbf{X} \end{array} \right] \quad (1)$$

where α, β, γ weights the contribution of every individual field change, and η weights the gain in the strain energy. \mathbf{K} represents the deformable model stiffness matrix, and $\Delta \mathbf{X}$ the deformable model node displacement vector. Analyzing Equation 1 we see that any change in the image fields or in the mesh point distribution will increase the system's total energy. Therefore, using the above energy definition, we state that the point correspondence from g_n to g_{n+1} is given by the mesh configuration whose total energy variation is the minimum. That means, the point correspondence is given by:

$$\hat{\mathbf{X}} = \mathbf{X} + \Delta \hat{\mathbf{X}}, \quad (2)$$

where

$$\Delta \hat{\mathbf{X}} = \min_{\Delta \mathbf{X}} \Delta U_n(\Delta \mathbf{X}) \quad (3)$$

If we set $\beta = 0$ and $\gamma = 0$, our problem corresponds to finding the optical flow of the node mesh under the minimum-mesh-deformation constraint. Therefore, the proposed motion-tracking algorithm can be used to find the optical flow of every voxel in the image given its segmentation.

2.1. Mesh Node Selection

Although Equation (2) can be used to estimate the motion of every voxel in the image, the number of voxels $\geq 10^6$ and the complex nature of the equation make its global minimization difficult. To simplify the problem, we opted to initially construct a coarse mesh using selected points from the image. Each selected point, became a node of the

$k^{l,m}$	Humeral head	muscle	tendon	cartilage
Humeral head	10^4	0.15	0.7	0.01
muscle	0.15	0.1	0.7	0.6
tendon	0.7	0.7	10^1	0.01
cartilage	0.01	0.6	0.01	10^2

Table 1. Relative stiffness and bounding stiffness of selected anatomical structures in the shoulder.

spring-mass mesh, where the node mass was a function of the tissue. Each node was attached to its closest nodes with a spring whose stiffness was defined by the material property of both nodes. Therefore, minimizing the energy of this coarse mesh will give us the motion of each one of its nodes.

The selection of those points is not trivial. First, for practical purposes the number of points has to be small $\simeq 10^4$. However, these selected points must be sufficient to describe the whole-image motion. Region boundaries are very important features because, for our motion tracking proposes, boundary tracking is enough for an accurate region motion description. Furthermore, interior points if they are far from the boundaries do not have sufficient information to be tracked,²¹⁻²³ but at region boundaries the magnitude of the gradient is high and the Laplacian is a zero crossing point, making them easy features to track. These facts compel the selection of segmented boundary points in the construction of our deformable model.

Although boundary points represent a small subset of the image points, there are still too many for practical proposes. To reduce the number of points we decided to use constrained random sampling of the boundary points for the point extraction step. The constraint consisted of avoiding the selection of a point too close to the ones already selected. This constraint allows a more uniform selection of the points around the boundaries. Finally, to reduce the motion estimation error at region internal points, and to make the mesh dynamics more stable, we randomly selected a few more points from the image using the same distance constraint. Experimental results show us that between 5,000 and 10,000 points are enough to estimate and describe the motion on a typical volumetric image of 256x256x34 voxels.

2.2. Deformable Model Mesh Construction

Once we have selected an appropriate set of feature points to track, the next step is the construction of a deformable model mesh from those points. This mesh constrains the kind of motion allowed by coding the material properties and the different interactions among regions. The first step in the mesh construction is to find for every nodal point, the neighboring nodal points. This corresponds to compute the Voronoi diagram of the mesh. Its dual, the Delaunay triangulation, represents the best possible tetrahedra tessellation for a given node configuration.²⁴ Although we can compute the Voronoi map for a N -nodes mesh with a $O(N \log(N))$ algorithm, we also need to know the closest node points for every voxel in the image, and we have to constrain this mesh in such a way to preserve the individual region topology. Therefore, we opted a simple constrained dilation approach for the construction of the Voronoi digram. The dilatation approach dilates every nodal point in the discrete volume constrained to the region it belongs. This is an improvement over the previous approach proposed by Tamez-Peña.⁷ The dilatation stops when it enter in contacts other dilated nodes. This procedure at the same time labels every voxel in the image with the corresponding closest nodal point of the mesh. Once every point \mathbf{x}_i has found each neighboring \mathbf{x}_j a spring is attached to each point pair with constant $k_{i,j}^{l,m}$, which defines the average iteration between material l and material m . The spring stiffness $k_{i,j}^{l,m}$ is defined by the material properties of the connected points. This properties are predefined by the user. If the connected points belong to the same region then the stiffness constant $k_{i,j}^{l,l}$ is related to the material elasticity properties; while $k_{i,j}^{l,m}$ for different material codes the average iteration between both at boundaries. Table I shows typical input data which defines the iteration between components. Although, in theory, we must define all the iteration between all adjacent regions; in practice we just define the interaction between the major anatomical components in the image, and the rest are left as an arbitrary small constant. This arbitrary selection makes the motion estimation less accurate; but the introduced error is not significant compared to other induced errors in our assumptions.

3. ENERGY MINIMIZATION

The problem of minimizing U can be addressed by dividing the problem into two units: rigid motion estimation and deformable motion estimation. Both use the same energy function but its minimization is addressed using different strategies. The rigid-motion-estimation-minimization strategy uses the fact that the mesh deformation energy $(\Delta \mathbf{X}^T \mathbf{K} \Delta \mathbf{X})/2$ is zero. From the segmentation, and our *a priori* knowledge of the anatomy we know which points belong to a rigid body. If we select those points for every individual rigid region then the rigid motion energy minimization problem is equal to finding the rigid motion rotation \mathbf{R}_i and translation \mathbf{T}_i that minimize every region's own external energy:

$$\begin{aligned} \Delta \hat{\mathbf{X}}_{rigid} &= \min_{\Delta \mathbf{X}} U_{rigid} \\ &= \sum_{\forall i \in rigid} (\Delta \hat{\mathbf{X}}_i = \min_{\Delta \mathbf{X}_i} U_n(\Delta \mathbf{X}_i)), \end{aligned} \quad (4)$$

where

$$\Delta \mathbf{X}_i = \mathbf{R}_i \mathbf{X}_i + \mathbf{T}_i - \mathbf{X}_i \quad (5)$$

and $\Delta \hat{\mathbf{X}}_i$ is the optimum displacement matrix of the points that belong to a rigid body R_i . This minimization problem has only six degrees of freedom for every rigid body: three in the rotation matrix and three in the translation matrix. Therefore, the 12 coefficients (9 rotation parameters, 3 translations) can be found via a 6 dimensional steepest descent technique if the difference between every two sequences is small enough.

Once we have found the rigid motion parameters, we proceed to estimate deformable motion throughout the minimization of the total system energy U . This problem cannot be simplified as much as the rigid motion case; and without further considerations the number of degrees of freedom in a 3D deformable object is $M = 3 * N$ where N is the number of node points in all the mesh. The physical nature of the problem allows the use of a simple gradient decent technique for each node in the mesh. From the potential and kinetic energies the Lagrangian of the system can be used to found the Euler-Lagrange equations for every node of the system. Furthermore, the driving local force is just the gradient of the energy field. For every node in the mesh, its local energy is given by:

$$\begin{aligned} U_{(\mathbf{x}_i),n}(\Delta \mathbf{x}) &= [\alpha(g_n(\mathbf{x}_i + \Delta \mathbf{x}) - g_{n+1}(\mathbf{x}_i))^2 \\ &\quad + \beta(\|\nabla g_n(\mathbf{x}_i + \Delta \mathbf{x})\| - \|\nabla g_{n+1}(\mathbf{x}_i)\|)^2 \\ &\quad + \gamma(\nabla^2 g_n(\mathbf{x}_i + \Delta \mathbf{x}) - \nabla^2 g_{n+1}(\mathbf{x}_i))^2 \\ &\quad + \eta \frac{1}{2} \sum_{\mathbf{x}_j \in \mathcal{G}_m(\mathbf{x}_i)} k_{i,j}^{l,m} (\mathbf{x}_j - \mathbf{x}_i - \Delta \mathbf{x})^2] \end{aligned} \quad (6)$$

where \mathcal{G}_m represents a neighborhood in the Voronoi diagram.

Therefore, every process handles a three-degrees-of-freedom problem whose minimization is performed using a simple gradient descent technique that iteratively reduces the local node energy. The local node gradient descent equation is

$$\mathbf{x}_i(n+1) = \mathbf{x}_i(n) - \nu \nabla U_{(\mathbf{x}_i(n),n)}(\Delta \mathbf{x}), \quad (7)$$

where the gradient of the mesh energy is analytically computable, the gradient of the field energy is numerically estimated from the image at different resolutions, $\mathbf{x}(n+1)$ is the next node position and ν weights the gradient contribution. Usually this process is done at three resolutions, where the image resolutions are computing by convolving the image with a Gaussian low pass filter with a different standard deviation.

At every step in the minimization, each process takes into account the neighboring nodes former displacement found for every other node in the mesh. The process is repeated until the total energy gets into a local minimum, which for small deformations is close to (or is) the global minima. The displacement vector found represents the estimated motion at the node points.

4. DENSE MOTION FIELD ESTIMATION

The node displacement $\Delta \mathbf{X}$ found in the minimization process is used to estimate the dense-motion-field needed to track the segmentation from one frame to the next. The dense-motion estimation is found by weighting the contribution of every neighbor node in the mesh. Assuming a constant velocity model, let us call $\mathbf{v}(\mathbf{x}, t) = \Delta \mathbf{x}(t)/\Delta t$ the estimated velocity at voxel \mathbf{x} at time t . Then, the dense motion field is estimated by:

$$\mathbf{v}(\mathbf{x}, t) = \frac{c(\mathbf{x})}{\Delta t} \sum_{\forall \Delta \mathbf{x}_j \in \mathcal{G}_m(\mathbf{x}_i)} \frac{k^{l,m} \Delta \mathbf{x}_j}{|\mathbf{x} - \mathbf{x}_j|}, \quad (8)$$

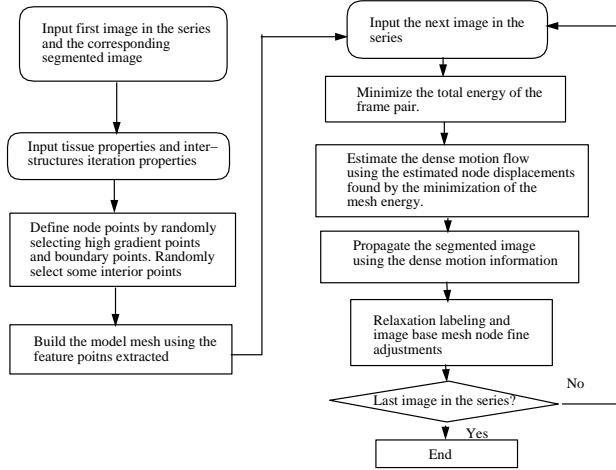


Figure 1. Motion tracking flow chart

where

$$c(\mathbf{x}) = \left[\sum_{\forall \Delta \mathbf{x}_j \in \mathcal{G}_m(x_i)} \frac{k^{l,m}}{|\mathbf{x} - \mathbf{x}_j|} \right]^{-1}, \quad (9)$$

$k^{l,m}$ the stiffness between material l and m associated to voxel \mathbf{x} and voxel \mathbf{x}_j respectively, ΔT the time between successive samples, $|\cdot|$ is a simple Euclidean distance, and the interpolation is done using the neighbor nodes of the closest node to the voxel \mathbf{x} , where $\mathbf{x} \in \mathcal{V}_m(x_i)$. This interpolation weights the contribution of every neighbor node by its material property $k_{i,j}^{l,m}$. Thus, the estimated voxel motion is similar for every homogeneous region even at the region's boundary.

To fill the next volume in the series with the segmented data at time $(t + \Delta t)$, we need the estimated velocity for every voxel in the next volume. That means that we need a reverse mapping of the estimated motion, which is given by:

$$v(\mathbf{x}, t + \Delta t) = \frac{1}{H} \sum_{\forall [\mathbf{x}_j + v(\mathbf{x}_j, t)] \in \mathcal{S}(\mathbf{x})} v(\mathbf{x}_j, t). \quad (10)$$

where H is the number of points that fall into the same voxel space $\mathcal{S}(\mathbf{x})$ in the next volume. This mapping, does not fill all the space at $t + \Delta t$; but a simple interpolation between mapped neighbor voxels can be used to fill out that space. Once we have an estimation of the velocity for every voxel in the next frame, its segmentation is simply:

$$L(\mathbf{x}, t + \Delta t) = L(\mathbf{x} - v(\mathbf{x}, t + \Delta t), t), \quad (11)$$

where $L(\mathbf{x}, t)$ is the label at voxel \mathbf{x} from the previous image, and $L(\mathbf{x}, t + \Delta t)$ is the voxel label at the new segmented image.

4.1. Error Correction

The motion tracking algorithm is as good as the initial assumptions. Therefore, it is not error free. Some of the errors can be corrected using the raw data once we have transferred all the label from one frame to the next. The error-correction step uses a simple approach. It assumes that the true segmentation can be recovered from the image given the initial segmentation using a relaxation algorithm. Therefore we relaxed the estimated segmentation *via* a deterministic relaxation algorithm like the one proposed by Pappas.²⁵ A boundary node point can be placed at the interior of a region after the relaxation; therefore it has to be adjusted. We adjust these boundary points by finding the boundary position that minimizes the deformation of the mesh. Figure 1 shows the flow chart of the motion tracking algorithm.

From frame	Difference PSNR	Warped PSNR	From frame	Difference PSNR	Warped PSNR	From frame	Difference PSNR	Warped PSNR
1 to 2	27.593	35.101	1 to 2	22.684	30.071	1 to 2	20.022	26.524
2 to 3	28.855	34.979	2 to 3	29.277	32.358	2 to 3	21.919	28.869
3 to 4	29.665	35.709	3 to 4	26.567	26.482	3 to 4	20.549	27.049
4 to 5	30.204	36.074	4 to 5	32.292	34.132	4 to 5	21.486	27.074
5 to 6	30.768	36.486	5 to 6	22.631	26.743	5 to 6	19.706	25.356
6 to 7	31.327	37.059	6 to 7	20.350	22.768	6 to 7	19.804	23.593
7 to 8	31.950	37.147	7 to 8	31.950	37.147			

Table 2. Peak signal to noise ratios (PSNR) analysis a) Phantom. b)Shoulder c) Knee

5. RESULTS

Our 4D-analysis approach has been used to analyze the motion of several MRI-volumetric-image sequences. But first the algorithm was validated by testing its reliability and performance on synthetic images generated by the deformation of a knee phantom. The phantom was modeled using a spring-mass model that had rigid and non-rigid components. The lower limb of the phantom was flexed from 0 degrees to a total flexion of 48 degrees in seven-degree increments. Figure 2 shows a single slice of the sequence and the comparison results. The synthetic image modeled a fat suppression MRI image, with a very low contrast. We created this image to test the algorithm performance on low contrast edges. The peak signal to noise ratio(PSNR) of the noise added to the image was 36 DB. The results show that the algorithm made a few errors on the region boundaries, and the errors became larger as the algorithm advanced on the sequence. Table 5a) shows the Peak signal to noise ratio comparisons between the frame difference and the difference between the image reconstructed from the estimated motion vectors obtained from the motion tracking algorithm (Warped image). The algorithm on average improved the PSNR to 36 DB, that is the noise power.

5.1. Four-Dimensional Shoulder

The algorithm performance on real data first was tested on a simple anatomical structure as the shoulder. Using the optimized imaging sequence, a volunteer was imaged as she rotated her arm stepwise from the neutral position to the maximal-external rotation. A total of eight useful image sequences were acquired. Each image size was 256x256x28 voxels with a spatial resolution of 0.43x0.43x2.0 millimeters for each voxel. The left image in Fig. 3, shows a single slice of the shoulder image.

The top right image shown at Fig. 3 is the segmented image obtained by the segmentation algorithm. The region boundaries are shown on the left bottom image as a white overlaid over the raw data. This segmentation was used as an input for the motion estimation and tracking algorithm. The relative material properties were defined for each one of the major components in the image like bone and muscle. Once these parameters and the $\alpha, \beta, \gamma, \eta$ coefficients of the energy term were defined, the algorithm was run on the image sequence, where a set of 5,000 points were automatically selected for the motion estimation algorithm: 4,000 at boundaries and 1,000 elsewhere. The algorithm was able to estimate the rotation of the humeral head, as well the displacement of all the soft tissues that surround it. Finally, Fig. 4 shows a lateral view of the surface renderings of three frames of the sequence. The humeral head is in gray, the muscle tissue is a transparent light gray. Notice the difference in position of the humeral head throughout the sequence. Table 5b) shows a comparison of the frame difference PSNR and the difference between the estimate frame and the current frame PSNR.

5.2. Four-Dimensional Knee

The main purpose of the study was the analysis of the knee flexion. For this case a volunteer was imaged while he flexed the knee. The image acquisition was done in similar way, as in the shoulder case, where the volunteer moved place the leg at different angles, and at each angle a MR, GRE T2 weighted scan was performed, optimized to enhance the contrast between the meniscus and the surrounding tissue. Using this approach an image sequence was generate. The image sequence consisted of a set of six 60x256x256 voxels volumetric frames with a spatial resolution of 0.47x0.47x1.4 mm³. Figure 5a) shows a single slice of the first volume of the knee sequence while 5b) shows

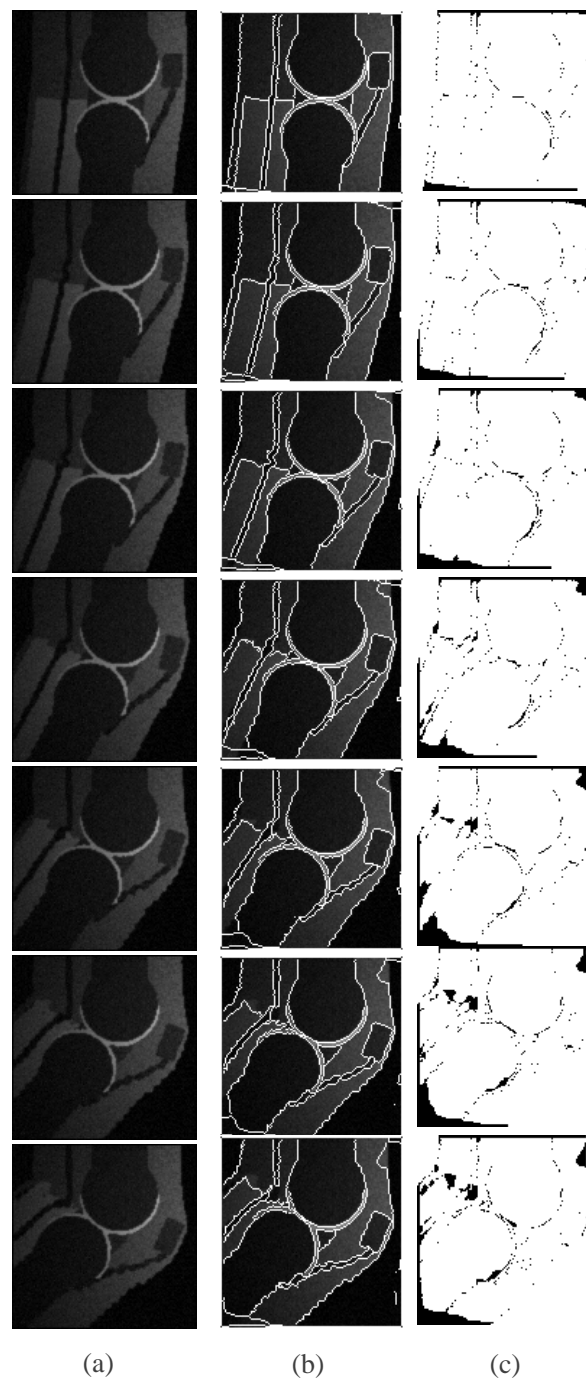


Figure 2. Tracking of the phantom data. (a) raw data sequence ,(b) Tracked boundaries over the raw data. (c) Tracking errors shown as black pixels

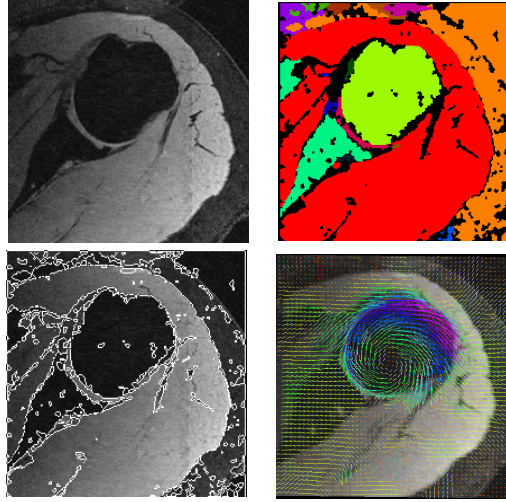


Figure 3. Single slice of segmentation of the 3D shoulder image. Left to right, top to bottom: original raw data, segmentation, regions boundaries overlaid over the raw data, motion flow vectors from frame 2 to 3

the segmentation boundaries overlaid the raw data. The algorithm was run on this sequence using similar energy coefficients as the ones used for the shoulder motion. Once the algorithm estimated the motion of every single voxel in the image on the sequence, it created the corresponding segmentation of the sequence. Table 5c) shows a PSNR comparison, of the frame difference and the PSNR of the warped image, notice the PSNR improvement. Figure 5c) shows the last frame of the sequence, and Fig. 5d) shows the warped segmented image boundaries overlaid over the image. The algorithm made a few errors while propagating the image. Figure 6 shows three of the reconstructed surfaces from the segmented image, where we can see the relative displacement of the patella and the motion of the muscle along the flexion. These reconstructions allowed us to create a movie and make some visual inspections of the knee motion, muscle deformation and meniscus behavior. Figure 7 shows the meniscus mesh and the tibia at the beginning of the knee flexion and at the end. We can see how this motion caused a small deformation of the meniscus mesh, however we are still trying to evaluate if this motion is valid or simply an artifact of the motion tracking algorithm.

A kinematic analysis of these data was performed on the femur and the medial meniscus. We computed for each structure of interest R_i its centroid and its main axis. We compute the centroid using only the N_i surface points Rs_i , of the structure R_i :

$$\mathbf{X}_i = \frac{1}{N_i} \sum_{\mathbf{x} \in Rs_i} \mathbf{x}, \quad (12)$$

The main axis orientation is given by the unitary vectors: $e_1, e_2, e_1 \times e_2$, where e_1 and e_2 are the two principal eigenvectors of the scattering matrix:

$$\mathbf{S}_i = \sum_{\mathbf{x} \in Rs_i} (\mathbf{x} - \mathbf{X}_i)(\mathbf{x} - \mathbf{X}_i)^T, \quad (13)$$

where \mathbf{x} and \mathbf{X}_i are column vectors. To make the kinematics analysis more robust to involuntary human motion, we set the tibia centroid and the tibia main axis orientation as our coordinate system. The relative centroid displacement of the femur, and the medial meniscus are shown in figures 8a) and 9a). As expected the relative motion of the femur with respect the tibia is quite large while the knee is undergoing flexion. The meniscus motion is very small. The range of displacement measured fall between the resolution of our system of $0.5 \times 0.5 \times 1.5$ mm, therefore we can not reach any conclusion from this data. The main axis rotation of the femur and the tibia can be seen on figures 8b) and 9b). These plots show clearly how the femur is rotating against the tibia along the segmented region main axis, which, in this case, is placed perpendicular to the long axis of the femur. Although the meniscus main axis show a small rotation, this rotation is very small and this rotation is close the measurement error. Further studies are required to verify if this rotation represents true physical events during flexion.

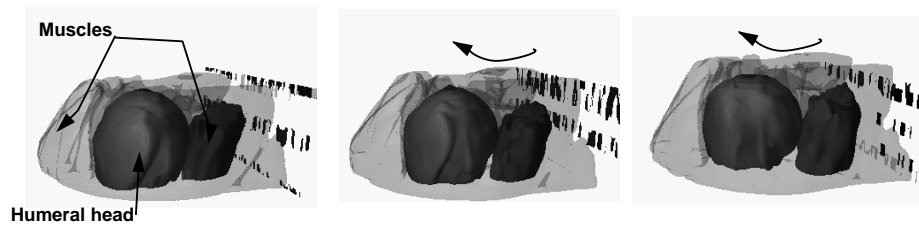


Figure 4. Rotating shoulder sequence. From left to right: surfaces renderings of frames 1,4 and 8.

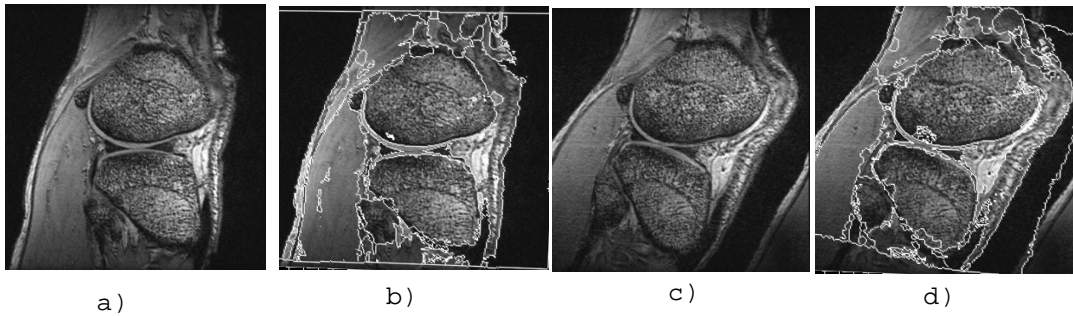


Figure 5. Single slice of segmentation of the 3D knee image. a) Raw data. b) Original regions boundaries overlaid over raw data. c) Frame 6 of the sequence. d) Warped segmentation boundaries overlaid over the data

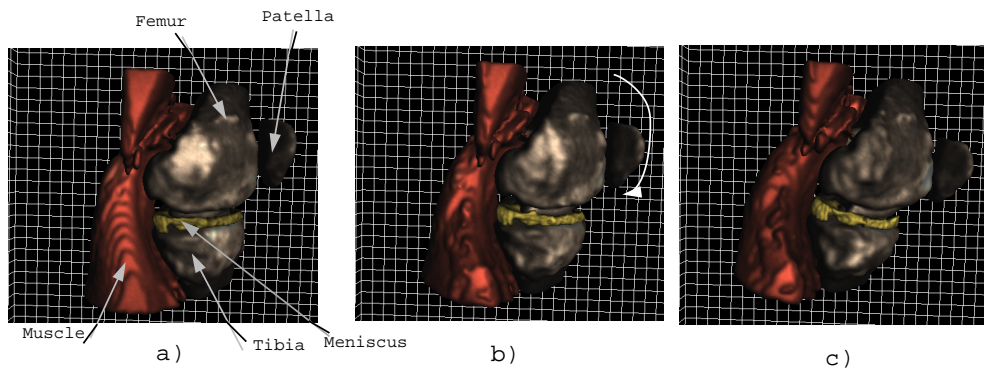


Figure 6. Surface renderings of the knee extension sequence. From left to right, side views of frames 1,3 and 6.

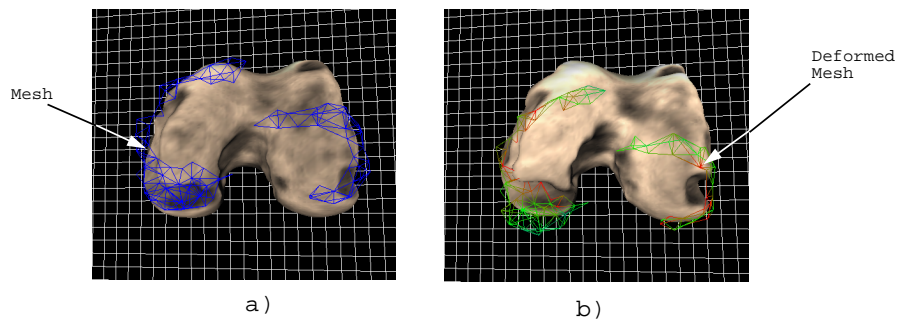


Figure 7. Meniscus mesh over the tibia. a) Undeformed starting mesh. b) Deformed mesh on the six frame of the sequence

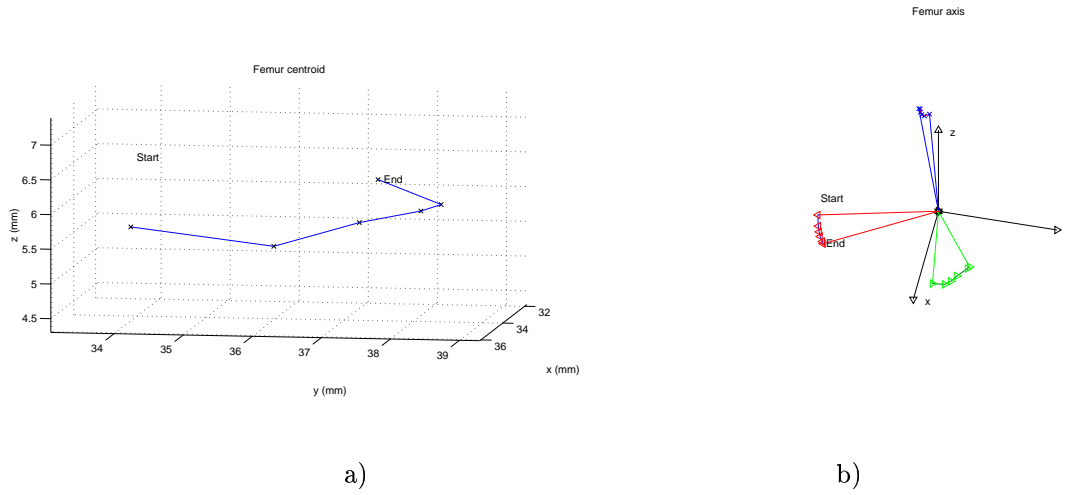


Figure 8. Relative femur motion against the tibia. a) Centroid displacement. b) main axis rotation

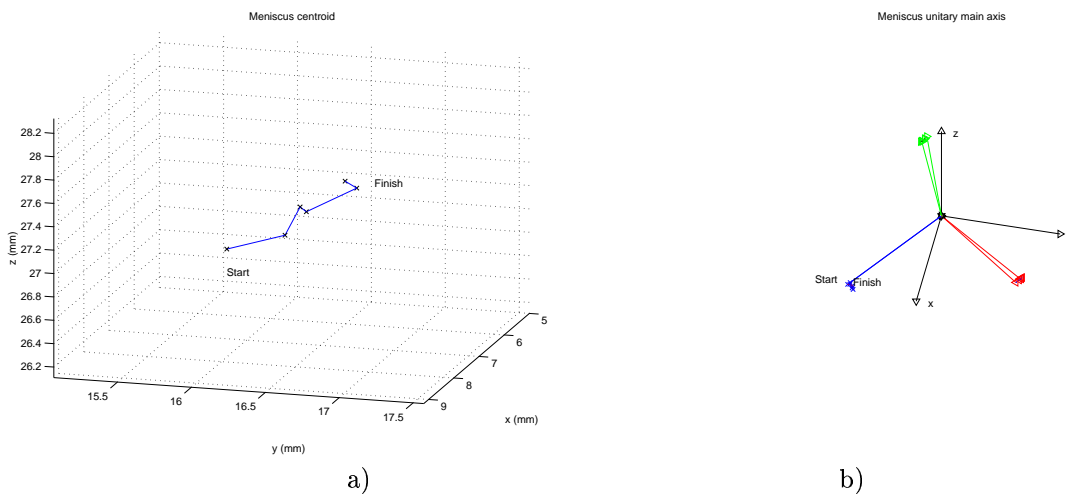


Figure 9. Relative medial meniscus motion against the tibia. a) Centroid displacement. b) main axis rotation.

The visualization of the volumetric data included including fat, muscle, bone, meniscus and cartilage and textured surfaces generated from the segmented data. The texture information was obtained from the original MR data by projecting the surrounding tissue density values into the surface. This approach enhances the visualization of the tendon-bone attachments and bone-cartilage contact points. The motion visualization was done by generating a series of movies which allowed a more vivid visualization of the iterations between different joint structures, where Fig. 6 and Fig. 4 show some frames of two of the generated movies.

6. CONCLUSION

We have presented an approach to the extraction and analysis of the major musculoskeletal structures from an set of MRI images, using a motion estimation and tracking algorithm. The algorithm performance was evaluated on a knee phantom and on a series of MRI sequences. A kinematic analysis of the extracted data was done on some knee structures: femur, tibia, patella, meniscus, cartilage. This paper presented the analysis of the femur and the medial meniscus. The relative path was displayed and analyzed along the knee flexion. The visualization of the data was enhanced by manually assigning display properties to each one of the major structures. This study is a step towards developing anatomic 3D kinematic models for all musculoskeletal structures. This is also a step towards the direction where patient specific 3D kinematic and biomechanical models can be developed and used in clinical practice. The direct kinematic patient specific data will, in the future, help us to better understand the mechanism behind the development of traumatic and degenerative osteoarthritic disorders and to plan approaches to prevent and treat them.

ACKNOWLEDGMENTS

This work is supported in part by the NSF/NYS Grant to the Center for Electronic Imaging Systems at the University of Rochester, the University of Rochester departments of Electrical Engineering and Radiology and by a Fulbright Scholarship from the U.S.A-Mexico Fulbright-CONACYT Commission, Mexico.

REFERENCES

1. D. Terzopoulos, A. Witkin, and M. Kass, "Constraints on deformable models: Recovering 3D shape and nonrigid motion," *Artificial Intelligence* **36**, pp. 91–123, 1988.
2. T. McInerney and D. Terzopoulos, "Dynamic finite element surface model for segmentation and tracking in multidimensional medical images with applications to cardiac 4D image analysis," *Computerized Medical Imaging and Graphics* **19**(1), pp. 69–83, 1995.
3. J. Park, D. Metaxas, A. Young, A. Alistair, and L. Leon, "Deformable models with parametric functions for cardiac motion analysis from tagged MRI data," *IEEE transactions on Medical Imaging* **15**(3), pp. 278–289, 1996.
4. J. C. McEachen and J. S. Duncan, "Shape-based tracking of left ventricular wall motion," *IEEE transactions on Medical Imaging* **17**(3), pp. 270–283, 1997.
5. C. Nastar and N. Ayache, "Frequency-based nonrigid motion analysis: application to four dimensional medical images," *IEEE transactions on Pattern Analysis and Machine Intelligence*, pp. 1067–1079, 1996.
6. J. Park, D. Metaxas, and L. Axel, "Analysis of left ventricular wall motion based on volumetric deformable models and MRI-SPAMM," *Medical Image Analysis* **1**(1), pp. 53–71, 1996.
7. J. G. Tamez-Peña, S. Totterman, and K. J. Parker, "The integration of automatic segmentation and motion tracking for 4D reconstruction and visualization of musculoskeletal structures," in *Proceedings IEEE Workshop on Biomedical Image Analysis*, pp. 154–163, IEEE, 1998.
8. M. Kass, A. Witkin, and D. Terzopoulos, "Snakes: Active contour models," *Int. J. Computer Vision*, pp. 32–331, 1988.
9. D. Terzopoulos and D. Metaxas, "Dynamic 3D models with local and global deformations: Deformable superquadrics," *PAMI* **13**(7), pp. 703–714, 1991.
10. S. Sclaroff and A. Pentland, "Modal matching for correspondence and recognition," *IEEE transactions on Pattern Analysis and Machine Intelligence* **17**(6), pp. 545–561, 1995.
11. A. C. B. K. A. Bartels and C. E. Griffin, "Spatio-temporal tracking of material shape change via multi-dimensional splines," in *Proceedings of IEEE Workshop on Biomedical Image Analysis*, pp. 110–116, IEEE, (USA), 1994.

12. D. Metaxas and D. Terzopoulos, "Constrained deformable superquadrics and nonrigid motion tracking," *IEEE Conf. on Computer Vision and Pattern Recognition*, pp. 337–343, June 1991.
13. J. S. Duncan, P. Shi, A. A. Amini, and et al., "Towards reliable, noninvasive measurement of myocardial function from 4D images," in *SPIE*, vol. 2168, pp. 149–161, SPIE, (USA), 1994.
14. C. Nastar and N. Ayache, "Classification of nonrigid motion in 3D images using physics-based vibration analysis," in *Proceedings of IEEE Workshop on Biomedical Image Analysis*, pp. 61–67, IEEE, (USA), 1994.
15. A. Matheny and D. Goldgof, "The use of three and four dimensional surface harmonics for nonrigid shape recovery and representation," *Trans. Patt. Anal and Mach. Intell* **17**(10), pp. 967–981, 1995.
16. M. Bro-Nielson, "Finite element modeling in surgery simulation," *Proceedings of the IEEE* **98**(3), pp. 490–503, 1998.
17. C. Kambhamettu and D. B. Goldgof, "Curvature-based approach to point correspondence recovery in conformal nonrigid motion," *CVGIP:Image Understanding* **60**(1), pp. 26–43, 1994.
18. J. C. M. II, A. Nehorai, and J. S. Duncan, "A recursive filter for temporal analysis of cardiac motion," in *Proceedings of IEEE Workshop on Biomedical Image Analysis*, pp. 124–133, IEEE, 1994.
19. J. Duncan, R. Owen, and P. Anandan, "Shape-based tracking of left ventricular wall motion," *Computers in Cardiology*, pp. 41–44, 1991.
20. J. G. Tamez-Peña, C. W. Chen, and K. J. Parker, "Local force model for cine CT cardiac dynamics analysis," in *SPIE Medical Imaging: Physiology and Function from Multidimensional Images*, vol. 3033, pp. 334–345, 1997.
21. B. K. P. Horn and B. G. Schunk, "Determining optical flow," *Artificial Intelligence* **17**, pp. 185–203, 1981.
22. A. M. Tekalp, *A. M. Digital Video Processing*, Prentice Hall, 1995.
23. D. Sim and R. Park, "Robust reweighted map motion estimation," *IEEE PAMI* **20**, pp. 353–365, 1998.
24. J. O'Rourke, *Computational Geometry in C*, Cambridge University Press, 1994.
25. T. N. Pappas, "An adaptive clustering algorithm for image segmentation," *IEEE Trans. Signal Proc.* **SP-40**, pp. 901–914, 1992.